Hacettepe Journal of Mathematics & Statistics

Hacet. J. Math. Stat.
Volume 54 (3) (2025), 998 – 1020
DOI : 10.15672/hujms.1659064

Research Article

Metric-based fuzzy rough sets for brain tumor magnetic resonance imaging classification

Manyu Cui[1], Fei Li *[1], Wei Yao[2], Guirong Peng[1]

[1] *College of Science, Beijing Forestry University, Beijing 100083, China.*
[2] *College of Science, Nanjing University of Information Science & Technology, Nanjing, 210044, China.*

Abstract

Computer-aided diagnosis systems help physicians diagnose diseases accurately at an early stage by automating preprocessing, image enhancement, and feature extraction, thus increasing patient survival rates. In this paper, we introduce an algorithm that leverages metric-based fuzzy positive regions to address the degradation of feature quality in brain tumor magnetic resonance imaging caused by inappropriate image enhancement. Employing sliding window blocks, the algorithm performs overlapping segmentation of magnetic resonance images and evaluates the membership of these blocks to decision classes by metric-based fuzzy positive regions. Blocks with the highest fuzzy positive region values are selected for multiple enhancement rounds, forming a candidate set that is sequentially integrated back into the original image. Finally, the features of the locally enhanced images are analyzed using the fuzzy positive region to generate the optimal feature set. To validate the effectiveness of the proposed algorithm, the features extracted using this method are compared with those extracted directly from the original image, globally enhanced images, and locally enhanced images processed based on similar fuzzy positive regions. The experimental results demonstrate that the proposed algorithm significantly outperforms the other three methods in various evaluation metrics, including the confusion matrix, classification accuracy, and the kappa coefficient.

Mathematics Subject Classification (2020). 03E72, 54A40

Keywords. Image processing, fuzzy rough sets, metric, fuzzy positive region, magnetic resonance imaging

1. Introduction

Brain tumors pose a serious threat to human health, accounting for more than 350,000 annual cases worldwide and are associated with a mortality rate of 2.5%. Magnetic resonance imaging (MRI) is commonly used in medicine to detect brain tumors, using contrast-enhanced scans to clearly highlight soft tissue and pathological areas of the brain [22]. Given the complexity of brain tumor types, precise diagnosis is heavily based on clinicians' expertise. To improve diagnostic precision, computer-aided diagnosis (CAD)

*Corresponding Author.
Email addresses: feifei_1004@bjfu.edu.cn (F. Li), cuimanyu@bjfu.edu.cn (M. Cui), yaowei@nuist.edu.cn (W. Yao), PPPPPPPGR@outlook.com (G. Peng)
Received: 16.03.2025; Accepted: 13.04.2025

systems [16,18,38,39] have been developed, which utilize machine learning or deep learning to train and analyze extracted image features, allowing automatic classification of different image types and detection of subtle changes during tumor growth that may not be visually apparent. For CAD systems, obtaining high-quality image features is crucial, as it directly impacts the model's classification performance. Generally, optimizing brain tumor MRI quality in CAD systems involves both image enhancement and feature extraction processes.

Image enhancement serves to improve image quality by boosting contrast and clarity, with the aim of highlighting target features for specific applications. Primary methods include histogram equalization, which adjusts the grayscale distribution to enhance contrast and clarity [48]; pulse-coupled neural network (PCNN) algorithms, which simulate interactions between neurons in the mammalian visual system to enhance contrast and details in similar grayscale areas [43]; wavelet transform algorithms, which decompose and adjust details and approximations of the image frequency to enhance detail and contrast [27]. Image enhancement strategies are typically divided into global enhancement [41,53] and local enhancement [30]. Local enhancement tends to preserve local details more effectively than global enhancement while improving contrast [13]. In brain MRI processing, global enhancement frequently fails to effectively highlight target features due to noise and the prevalence of soft tissue structures. In contrast, local enhancement targets specific areas, improving not only the clarity and contrast of these regions but also the integrity of surrounding tissues, thus maintaining the overall completeness of the image information.

Feature extraction primarily involves analyzing the color, shape, and texture characteristics of an image. Most medical images, including X-rays, CT scans, and MRI, are presented in gray-scale, primarily reflecting differences in tissue signal intensity. In grayscale images, texture features reveal the microstructure of tissues and are particularly sensitive to subtle pathological changes. These features can detect subtle changes in grayscale information before changes in shape or color become apparent at the lesion site. Thus, analyzing texture features in medical images is crucial for the early detection and diagnosis of diseases.

Fuzzy rough sets, which combine the advantages of fuzzy set theory and rough set theory, effectively handle the incompleteness and uncertainty inherent in continuous data without requiring prior domain knowledge, thereby demonstrating significant value across diverse applications. In feature selection and attribute reduction, fuzzy rough set-based methods identify essential features, remove redundancy, and improve classification efficiency, particularly in high-dimensional datasets such as genomic analysis, biomedical research, and text classification [17,26,54]. These techniques have been successfully applied to tumor classification through gene selection [17] and distributed feature selection in large-scale data processing [26]. Similarly, in pattern recognition and machine learning, fuzzy positive regions refine classification boundaries, leading to better decision-making and recognition accuracy in applications such as facial recognition, fingerprint identification, and speech recognition [1,5,10]. In addition, fuzzy rough sets play a critical role in image processing by enhancing feature extraction, segmentation, and classification, thus improving overall image analysis performance. Du et al. [14] optimized the process of feature extraction and selection for driver fatigue detection using fuzzy rough set techniques in the kernel. Yu et al. [42] developed an automatic class boundary detection algorithm using fuzzy rough sets, effectively resolving issues with overlapping intensity distributions in auroral oval images that complicate boundary separation. Chen et al. [9] improved the accuracy of land use classification in remote sensing images and reduced the count of features using domain-based fuzzy rough set technology, overcoming the limitations of traditional maximum likelihood classification methods in 2020. Qu et al. [36] improved the classification accuracy in breast X-ray photography by extracting high-quality features with fuzzy rough sets. All of these image-processing studies utilized fuzzy rough set models that focused on

the similarity between elements. Yao et al. [51,52] integrated a hemimetric function into fuzzy rough sets to delineate distant relationships between elements, thereby enhancing the differentiation of disparities among them. In medical image diagnostics, the main analysis focuses on the disparities in texture, density, and signal intensity between the lesion areas and adjacent normal tissues. Compared to similarity-based fuzzy rough sets, the distance function directly quantifies differences between elements, offering a more direct and flexible approach. This method enables a more precise differentiation of regions that are visually subtle but exhibit significant discrepancies in image characteristics relative to surrounding tissues.

Based on the preceding analysis, we construct a metric-based fuzzy positive region (MFPR) by analyzing metric-based fuzzy rough sets. In addition, we propose an algorithm that uses MFPR to optimize the quality of MRI features for brain tumors. The algorithm employs a sliding window method [11] to perform overlapping segmentation on MRI and extracts texture features from each window block using a gray-level co-occurrence matrix (GLCM) [24]. Then, a PCNN was used to perform multiple rounds of enhancement on the window block with the highest MFPR value, forming a candidate set of enhanced results [34, 49]. Note that the value of the fuzzy positive region quantifies the importance of each window block in decision-making [8]. Furthermore, these enhanced blocks are then sequentially embedded in the original image, and the features of the locally enhanced image with the highest MFPR value are selected to form the optimal feature set. In the experimental section, the comparison algorithms include feature extraction based on the original image, global enhancement (GE), and fuzzy positive region (SFPR) window enhancement based on similarity. We employ twelve commonly used classifiers to comprehensively analyze the experimental results using three metrics: confusion matrix [35], classification accuracy, and kappa coefficient [46]. The results demonstrate that the MFPR algorithm outperforms other methods in most classification models. In addition, the experimental section analyzes the classification performance of the algorithm under different window sizes to verify its general applicability.

The remainder of this paper is organized as follows. The fundamental theoretical concepts are introduced in Section 2. The construction process of the MFPR and its properties, together with the corresponding proofs, are explained in Section 3. The specific implementation process of the MFPR algorithm for optimizing the features of the image is described in Section 4. The experimental results are analyzed in Section 5. The paper concludes in Section 6 with a discussion of the challenges in this research field and future research directions.

2. Background

This section introduces the method of using the GLCM to extract image texture features and explains the principle of using PCNN for image enhancement.

2.1. Gray-level co-occurrence matrix

The GLCM is a tool that characterizes the texture of an image by analyzing pixel pairs at various distances d and angles θ. This method quantifies the gray-scale variation of image pixels at multiple scales and orientations while analyzing the spatial distribution patterns of gray-level values [24]. From the GLCM, texture features such as correlation, contrast, entropy, angular second moment, and inverse difference moment are extracted to characterize texture information in the image [28]. These features are widely used in fields such as image analysis, target recognition, and classification [15,40]. In the calculation of the GLCM, the parameter d is generally set to 1, and θ is selected as 0°, 45°, 90°, and 135° to capture the predominant texture orientations within the image, as shown in Figure 1. The process of generating the GLCM is illustrated in Figure 2. Figure 2 (a) contains 5

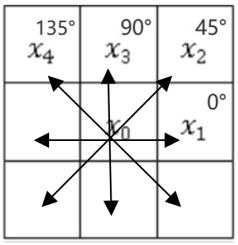

Figure 1. Illustration of pixel distance $d = 1$ and angles 0°, 45°, 90°, and 135°.

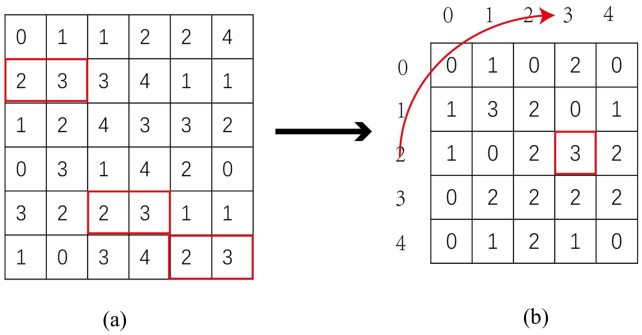

Figure 2. Example of GLCM generation with $d = 1$ and $\theta = 0°$. (a) Gray-scale image. (b) Gray-level co-occurrence matrix.

gray levels, resulting in a matrix 5×5 as seen in Figure 2(b), where each element $G(i, j)$ in the matrix represents the number of times the gray levels i and j cooccur at a distance of $d = 1$ and an angle of $\theta = 0°$. For example, in Figure 2(a), the ordered pairs with gray-levels 2 and 3 appear horizontally adjacent three times, indicating that $G(2, 3) = 3$ in Figure 2(b).

2.2. Pulse coupled neural network

The PCNN captures pixels with similar gray values by simulating the interactions between neurons in the mammalian visual system [34,49]. PCNN is widely applied in image processing tasks such as image segmentation, texture analysis, image enhancement, and pattern recognition [31,50]. This technique can enhance image brightness, improve contrast and details, and highlight essential texture features. In this study, PCNN is utilized to enhance images by highlighting the texture features of critical information.

The PCNN consists of a single-layer, two-dimensional array of neurons, each corresponding to a pixel in the input image [25]. Specifically, the neuron N_{ij} in the array corresponds to the (i, j) pixel of the image. Each neuron in PCNN comprises three main components: a signal input domain, a non-linear modulation domain, and a pulse generation domain [29], as seen in Figure 3.

2.2.1. Signal input domain. The input signals primarily consist of feedback inputs F_{ij} and linking inputs from neighboring neurons L_{ij}, both of which are represented as matrices with i rows and j columns. At the n-th pulse firing, the expressions for $F_{ij}[n]$ and $L_{ij}[n]$ are as follows:

$$F_{ij}[n] = S_{ij}[n]; \tag{2.1}$$

$$L_{ij}[n] = e^{-\alpha_L} L_{ij}[n-1] + V_L \sum_{kl} W_{ijkl} Y_{kl}[n-1]. \tag{2.2}$$

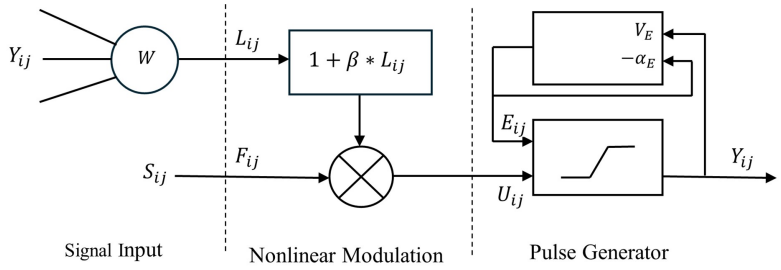

Figure 3. A PCNN neuron model.

In this context, S_{ij} represents the normalized grayscale input image, $Y_{kl}[n-1]$ is the pulse output of the neighboring neuron (k,l) at the $(n-1)$th firing time, which can be 0 or 1. The definition of Y_{kl} is given in (2.4). W_{ijkl} represents the weight matrix of the connection between neurons, while α_L and V_L correspond to the time decay constant and the inherent potential of L_{ij}, respectively.

2.2.2. Nonlinear modulation domain. The internal excitation voltage U_{ij} of the neuron (i, j), resulting from the coupling, is influenced by the pulse firing of neighboring neurons. The value of U_{ij} is determined through nonlinear modulation involving F_{ij} and L_{ij}, as defined by the following equation:

$$U_{ij}[n] = F_{ij}[n](1 + \beta L_{ij}[n]), \tag{2.3}$$

where β is the connection strength coefficient between neighboring neurons.

2.2.3. Pulse generation domain. In this module, the generation of the time series pulse sequence Y_{ij} depends on the magnitude of U_{ij} and the dynamic threshold voltage E_{ij}, as shown in (2.4). (2.5) describes the dynamic change process of the threshold voltage [56]:

$$Y_{ij}[n] = \begin{cases} 1, & U_{ij}[n] > E_{ij}[n]; \\ 0, & \text{otherwise.} \end{cases} \tag{2.4}$$

$$E_{ij}[n] = e^{-\alpha_E} E_{ij}[n-1] + V_E Y_{ij}[n]. \tag{2.5}$$

The neuron (i,j) produces a low level when E_{ij} exceeds U_{ij}, causing the pulsing domain to stop, i.e. $Y_{ij} = 0$. Subsequently, it E_{ij} decays exponentially according to the threshold decay constant α_E, which determines the decay rate, until E_{ij} falls below U_{ij} again, triggering the next firing event. The algorithm iteratively cycles through (2.1) to (2.5), forming a pulse sequence. The number of firings can be predefined [12].

The principle of image enhancement is expressed in (2.6):

$$\mathrm{Enh}S_{ij}[n] = (\ln(\mathrm{Bri}) - \alpha_E(n-1))Y_{ij}[n], \tag{2.6}$$

where $\mathrm{Enh}S_{ij}$ represents the enhanced gray-scale image, and Bri denotes the maximum pixel value in the input image [21]. It is evident from the equation above that different values of α_E correspond to different enhancement effects.

3. Metric-based fuzzy positive region and properties

Previous fuzzy rough set models, using binary relations, neighborhood operators, and coverings, have proven effective in characterizing specific proximity relationships between data sets [4, 19, 37, 44]. Beyond these relation-based methods, a distance function, formally known as a metric in mathematics, provides a numerical measure of separation or dissimilarity between objects. Smaller values indicate greater similarity, while larger values signify greater differences. In contrast to tosimilarity-based fuzzy rough sets, distance

functions offer a more direct and flexible means of quantifying disparities between elements, enabling the detection of subtle variations that traditional relation-based methods may overlook.

Motivated by this perspective, this section develops fuzzy upper and lower approximation operators based on metric functions using metric functions. Furthermore, the fuzzy positive region is constructed systematically and its essential properties are rigorously analyzed.

3.1. Hemimetric-based fuzzy rough approximation operators

A hemimetric [20] is a variation of a traditional metric that allows for asymmetry. Based on this concept, Yao et al. [51] constructed a fuzzy rough set model based on hemimetrics to describe similarity or dissimilarity between elements.

Definition 3.1 ([20])**.** For a non-empty set X, a function $d : X \times X \to [0, +\infty)$ is called a hemimetric if

$$d(x, x) = 0, for\ \forall x \in X; \tag{3.1a}$$

$$d(x, z) \leq d(x, y) + d(y, z), for\ \forall x, y, z \in X. \tag{3.1b}$$

The pair (X, d) is called a hemimetric space. The function d represents a distance or degree of separation between elements in the set X, constituting a non-symmetric version of the standard metric. If $d(x, y) = d(y, x)$ holds for every $x, y \in X$, then d is considered symmetric. Specifically, property (3.1a) indicates that the distance function satisfies reflexivity, meaning the distance from any point to itself is zero. The property (3.1b) is similar to the triangle inequality in metric spaces, ensuring the consistency and stability of d. Based on these properties, a pair of fuzzy rough approximation operators is constructed within the hemimetric space.

Definition 3.2 ([52])**.** Let (X, d) be a hemimetric space. A function $A : X \to [0, 1]$ is a fuzzy subset of X. For any $x \in X$, $A(x)$ represents the membership degree of x in A. Let $F(X) = \{A_i \mid i \in I\}$ be the collection of all fuzzy subsets. Then, the fuzzy lower and upper rough approximation operators $\underline{Apr}_d$, $\overline{Apr}_d : F(X) \to F(X)$, induced by the hemimetric d, are defined as follows:

$$\underline{\mathrm{Apr}}_d(A)(x) = \bigwedge_{y \in X} (A(y) + d(x, y)); \tag{3.2a}$$

$$\overline{\mathrm{Apr}}_d(A)(x) = \bigvee_{y \in X} (A(y) - d(y, x)). \tag{3.2b}$$

In particular, the asymmetry of the hemimetric d introduces a directional dependency on the input arguments x and y, which must be carefully considered when defining fuzzy rough approximation operators. Although hemimetrics offer flexibility in modeling asymmetry in fuzzy rough set theory, their directional dependency limits their applicability in domains such as medical imaging, where anatomical consistency requires a distance function that satisfies metric properties, including symmetry $d(x, y) = d(y, x)$. To address this limitation, we introduce a metric-based fuzzy decision system to ensure symmetry, with the aim of simplifying theoretical analysis and computational processes.

3.2. Metric-based fuzzy decision system and metric-based fuzzy positive region

The traditional metric definition allows the values to extend indefinitely. In this study, we focus on fuzzy rough sets where membership degrees are restricted to the $[0, 1]$ interval. To ensure accurate data processing, the original attribute values are first fuzzified

and mapped to the $[0, 1]$ range through a normalization process. Building on this foundation, we introduce a metric function to define a new fuzzy metric relation, quantify data differences, and build a metric-based fuzzy decision system.

Definition 3.3. In a fuzzy information system (U, A), let U denote the universe, and let $A = \{b_1, b_2, \ldots, b_n\}$ be the set of condition attributes. For each attribute $b \in A$, let d_b be the metric function, where $d_b(x, y)$ measures the degree of dissimilarity between objects x and y with respect to attribute b. Then, the fuzzy metric relation of an attribute subset $B \subseteq A$ is defined by

$$d_B(x, y) = \bigvee_{b \in B} d_b(x, y), \ \forall x, y \in U. \tag{3.3}$$

Now, we investigate the properties of the fuzzy metric relation on U.

Theorem 3.4. *Let (U, A) be a fuzzy information system. Then for $B \subseteq A$, it holds that*

$$d_B(x, x) = 0, \ \forall x \in U; \tag{3.4a}$$
$$d_B(x, y) = d_B(y, x), \ \forall x, y \in U; \tag{3.4b}$$
$$d_B(x, z) \leq d_B(x, y) + d_B(y, z), \ \forall x, y, z \in U; \tag{3.4c}$$
$$d_{B_i} \leq d_{B_j}, if \ B_i \subseteq B_j \subseteq A. \tag{3.4d}$$

Proof. It is obvious that (3.4a) and (3.4b) are satisfied, here we only prove (3.4c) and (3.4d).

(3.4c) For every $x, y, z \in U$,

$$\begin{aligned} d_B(x, y) + d_B(y, z) &= \bigvee_{b \in B} d_b(x, y) + \bigvee_{b \in B} d_b(y, z) \\ &= \bigvee_{b \in B} (d_b(x, y) + d_b(y, z)) \\ &\geq \bigvee_{b \in B} d_b(x, z) \\ &= d_{_B}(x, z). \end{aligned}$$

(3.4d) For $B_i \subseteq B_j \subseteq A$, $\forall x, y \in U$,

$$d_{B_i}(x, y) = \bigvee_{b \in B_i} d_b(x, y) \leq \bigvee_{b \in B_j} d_b(x, y) = d_{B_j}(x, y).$$

□

Properties (3.4a)-(3.4c) indicate that d_B satisfies the conditions of a metric. Property (3.4d) demonstrates the monotonicity of the fuzzy metric function with respect to the expansion of the set of attributes. This property is particularly useful for attribute importance analysis, feature selection, and pattern recognition, as it helps optimize fuzzy decision system construction and improves computational efficiency. Based on d_B, the fuzzy lower and upper rough approximation operators are defined as follows:

Definition 3.5. Let (U, A, D) be a fuzzy decision system, where A is the set of condition attributes and D is the set of decision attributes. The partition of U induced by D is denoted as $U/D = \{[x]_D \mid x \in U\} = \{D_1, D_2, \ldots, D_l\}$, where $[x]_D$ represents the decision class containing the object x. For each decision class $D_i \subseteq U/D$ and $B \subseteq A$, the metric-based fuzzy rough approximation operators are given by

$$\underline{\mathrm{Apr}}_{d_B}(D_i)(x) = \bigwedge_{y\in U}(D_i(y) + d_B(x,y)); \tag{3.5a}$$

$$\overline{\mathrm{Apr}}_{d_B}(D_i)(x) = \bigvee_{y\in U}(D_i(y) - d_B(x,y)). \tag{3.5b}$$

where the function

$$D_i(y) = \begin{cases} 1, & \text{if } y \in D_i; \\ 0, & \text{otherwise,} \end{cases}$$

represents the membership degree of y in the decision class D_i. Under the condition attributes, the fuzzy lower rough approximation operator $\underline{\mathrm{Apr}}_{d_B}(D_i)$ captures the extent to which x definitively belongs to the decision D_i, while the fuzzy upper rough approximation operator $\overline{\mathrm{Apr}}_{d_B}(D_i)$ reflects the degree of potential membership. Since the positive region is constructed solely on the basis of $\underline{\mathrm{Apr}}_{d_B}(D_i)$, we focus on exploring the properties of $\underline{\mathrm{Apr}}_{d_B}(D_i)$ in the following discussion.

Theorem 3.6. *Let (U, A, D) be a fuzzy decision system, define $\bar{0}$ as a set where all elements have a membership degree of zero, while $\bar{1}$ represents a set where all elements have a membership degree of one. Then for all $D_i \in U/D$ and $B \subseteq A$, let D_0 and D_U denote the empty set and the universal set, respectively. The following properties hold:*

$$\bar{0} \le \underline{\mathrm{Apr}}_{d_B}(D_i) \le \bar{1}; \tag{3.6a}$$

$$\underline{\mathrm{Apr}}_{d_B}(D_0) = \bar{0};\ \underline{\mathrm{Apr}}_{d_B}(D_U) = \bar{1}; \tag{3.6b}$$

$$\underline{\mathrm{Apr}}_{d_B}(\bigwedge_i D_i) = \bigwedge_i \underline{\mathrm{Apr}}_{d_B}(D_i); \tag{3.6c}$$

$$\underline{\mathrm{Apr}}_{d_B}(\underline{\mathrm{Apr}}_{d_B}(D_i)) = \underline{\mathrm{Apr}}_{d_B}(D_i); \tag{3.6d}$$

$$\underline{Apr}_{d_{B_i}}(D_i)(x) = \begin{cases} \bigwedge\limits_{y\notin D_i} d_B(x,y), & x \in D_i \\ 0, & otherwise; \end{cases} \tag{3.6e}$$

$$\underline{Apr}_{d_{B_i}}(D_i) \le \underline{Apr}_{d_{B_j}}(D_i),\ \text{if} B_i \subseteq B_j \subseteq A. \tag{3.6f}$$

It is important to note that the properties analogous to Equations (3.6a)(3.6d) were established in [52] for the hemimetric case. In this work, we extend these results to the metric case, where the symmetry of the metric function imposes stricter constraints. Consequently, these properties are naturally maintained. Equation (3.6e) presents a simplified form of the definition of the fuzzy lower approximation operator. Here, we provide the proof only for Equation (3.6f).

Proof. By (3.4c), for $B_i \subseteq B_j \subseteq A$, $\forall x \in U$, we have:

$$\begin{aligned} \underline{Apr}_{d_{B_i}}(D_i)(x) &= \bigwedge_{y\in U}(D_i(y) + d_{B_i}(x,y)) \\ &\le \bigwedge_{y\in U}(D_i(y) + d_{B_j}(x,y)) \\ &= \underline{Apr}_{d_{B_j}}(D_i)(x). \end{aligned}$$

□

Property (3.6f) indicates that the fuzzy lower rough approximation operator possesses a monotonically non-decreasing characteristic as the attribute subsets expand. This implies that larger attribute subsets yield stronger certainty lower bounds, potentially enhancing the approximation capability for decision classes.

Table 1. An example of fuzzy information systems

U	b_1	b_2	b_3	b_4	D_1	D_2
x_1	0.1	0.5	0.6	0.6	1	0
x_2	0.3	0.6	0.7	0.4	1	0
x_3	0.6	0.2	0.4	0.4	1	0
x_4	0.9	0.4	0.2	0.7	0	1
x_5	0.8	0.8	0.5	0.1	0	1
x_6	0.6	1.0	0.3	0.2	1	0

Definition 3.7. Let (U, A, D) be a fuzzy decision system, for all $D_i \in U/D$, $B \subseteq A$ and $x \in U$, the metric-based fuzzy positive region (MFPR) is defined by

$$Pos_{d_B}(D)(x) = \bigvee_{i=1}^{l} \underline{Apr}_{d_B}(D_i)(x). \tag{3.7}$$

The MFPR, defined as the supremum ($\bigvee$) of fuzzy lower rough approximation operators across all decision classes D_i, quantifies the certainty of an element's membership to the decision classes under the metric relation d_B. A higher value of the fuzzy positive region signifies a stronger correlation between the element and the decision.

Example 3.8. Let (U, B, D) be a fuzzy decision system, as shown in Table 1. Here, $U = \{x_1, x_2, x_3, x_4, x_5, x_6\}$, $B = \{b_1, b_2, b_3, b_4\}$, and $U/D = \{D_1, D_2\}$, where $D_1 = \{x_1, x_2, x_3, x_6\}$ and $D_2 = \{x_4, x_5\}$. Let $d_b(x, y) = |b(x) - b(y)|$ for every $x, y \in U$. It is evident that $d_b(x, y)$ is a metric function. The metric relationship of elements in the dataset under each attribute b_i is as follows:

$$d_{b_1}(x,y) = \begin{pmatrix} 0.0 & 0.2 & 0.5 & 0.8 & 0.7 & 0.5 \\ 0.2 & 0.0 & 0.3 & 0.6 & 0.5 & 0.3 \\ 0.5 & 0.3 & 0.0 & 0.3 & 0.2 & 0.0 \\ 0.8 & 0.6 & 0.3 & 0.0 & 0.1 & 0.3 \\ 0.7 & 0.5 & 0.2 & 0.1 & 0.0 & 0.2 \\ 0.5 & 0.3 & 0.0 & 0.3 & 0.2 & 0.0 \end{pmatrix} \tag{3.8}$$

$$d_{b_2}(x,y) = \begin{pmatrix} 0.0 & 0.1 & 0.3 & 0.1 & 0.3 & 0.5 \\ 0.1 & 0.0 & 0.4 & 0.2 & 0.2 & 0.4 \\ 0.3 & 0.4 & 0.0 & 0.2 & 0.6 & 0.8 \\ 0.1 & 0.2 & 0.2 & 0.0 & 0.4 & 0.6 \\ 0.3 & 0.2 & 0.6 & 0.4 & 0.0 & 0.2 \\ 0.5 & 0.4 & 0.8 & 0.6 & 0.2 & 0.0 \end{pmatrix} \tag{3.9}$$

$$d_{b_3}(x,y) = \begin{pmatrix} 0.0 & 0.1 & 0.2 & 0.4 & 0.1 & 0.3 \\ 0.1 & 0.0 & 0.3 & 0.5 & 0.2 & 0.4 \\ 0.2 & 0.3 & 0.0 & 0.2 & 0.1 & 0.1 \\ 0.4 & 0.5 & 0.2 & 0.0 & 0.3 & 0.1 \\ 0.1 & 0.2 & 0.1 & 0.3 & 0.0 & 0.2 \\ 0.3 & 0.4 & 0.1 & 0.1 & 0.2 & 0.0 \end{pmatrix} \tag{3.10}$$

$$d_{b_4}(x,y) = \begin{pmatrix} 0.0 & 0.2 & 0.2 & 0.1 & 0.5 & 0.4 \\ 0.2 & 0.0 & 0.0 & 0.3 & 0.3 & 0.2 \\ 0.2 & 0.0 & 0.0 & 0.3 & 0.3 & 0.2 \\ 0.1 & 0.3 & 0.3 & 0.0 & 0.6 & 0.5 \\ 0.5 & 0.3 & 0.3 & 0.6 & 0.0 & 0.1 \\ 0.4 & 0.2 & 0.2 & 0.5 & 0.1 & 0.0 \end{pmatrix} \tag{3.11}$$

Based on Equation (3.3), the metric relationship among elements under the attribute set B is obtained as follows:

$$d_B(x,y) = \begin{pmatrix} 0.0 & 0.2 & 0.5 & 0.8 & 0.7 & 0.5 \\ 0.2 & 0.0 & 0.4 & 0.6 & 0.5 & 0.4 \\ 0.5 & 0.4 & 0.0 & 0.3 & 0.6 & 0.8 \\ 0.8 & 0.6 & 0.3 & 0.0 & 0.6 & 0.6 \\ 0.7 & 0.5 & 0.6 & 0.6 & 0.0 & 0.2 \\ 0.5 & 0.4 & 0.8 & 0.6 & 0.2 & 0.0 \end{pmatrix} \tag{3.12}$$

Based on Equation (3.5a), the fuzzy lower approximation value for each element x is determined as follows:

$$\underline{\mathrm{Apr}}_{d_B}(D_1)(x) = (\ 0.7 \quad 0.5 \quad 0.3 \quad 0.0 \quad 0.0 \quad 0.2\ ) \tag{3.13}$$

$$\underline{\mathrm{Apr}}_{d_B}(D_2)(x) = (\ 0.0 \quad 0.0 \quad 0.0 \quad 0.3 \quad 0.2 \quad 0.0\ ) \tag{3.14}$$

Based on Equation (3.7), the following results can be derived:

$$Pos_{d_B}(D)(x) = (\ 0.7 \quad 0.5 \quad 0.3 \quad 0.3 \quad 0.2 \quad 0.2\ ) \tag{3.15}$$

From the calculations above, the maximum fuzzy positive region value for x_1 is 0.7, indicating that x_1 has the highest correlation with the decision. Next, we investigate theorems related to the MFPR.

Theorem 3.9. *Let (U, A, D) be a fuzzy decision system, for all $D_i \in U/D$ and $B \subseteq A$, let D_0 and D_U denote the empty set and the universal set, respectively. The following properties hold:*

$$Pos_{d_B}(D_i) = \underline{Apr}_{d_B}(D_i); \tag{3.16a}$$

$$Pos_{d_B}(D_0) = \bar{0};\ Pos_{d_B}(D_U) = \bar{1}; \tag{3.16b}$$

$$\bar{0} \le Pos_{d_B}(D) \le \bar{1}; \tag{3.16c}$$

$$Pos_{d_B}(Pos_{d_B}(D)) = Pos_{d_B}(D); \tag{3.16d}$$

$$Pos_{d_{B_i}}(D) \le Pos_{d_{B_j}}(D),\ if\ B_i \subseteq B_j \subseteq A; \tag{3.16e}$$

$$Pos_{d_B}(D_M) \le Pos_{d_B}(D_N),\ if\ D_M \subseteq D_N \subseteq U/D. \tag{3.16f}$$

Proof. It is evident that theorem (3.16a) and (3.16b) is satisfied. The proofs of theorems (3.16c)-(3.16f) are provided subsequently:

(3.16c) Clearly, $Pos_{d_B}(D) \ge \bar{0}$, for every $x \in U$,

$$Pos_{d_B}(D)(x) = \bigvee_{i=1}^{l} \underline{Apr}_{d_B}(D_i)(x) \le \bigvee_{i=1}^{l} (D_i)(x) = \bar{1}.$$

That is, $Pos_{d_B}(D) \le \bar{1}$.

(3.16d) For every $x \in U$,

$$\begin{aligned} Pos_{d_B}(Pos_{d_B}(D))(x) &= \underline{Apr}_{d_B}(Pos_{d_B}(D))(x) \\ &= \underline{Apr}_{d_B}(\bigvee_{i=1}^{l} \underline{Apr}_{d_B}(D_i))(x) \\ &= \bigvee_{i=1}^{l} \underline{Apr}_{d_B}(\underline{Apr}_{d_B}(D_i))(x) \\ &= \bigvee_{i=1}^{l} \underline{Apr}_{d_B}(D_i)(x) \\ &= Pos_{d_B} D(x) \end{aligned}$$

(3.16e) For every $B_i \subseteq B_j \subseteq B$ and $x \in U$,

$$\begin{aligned} Pos_{d_{B_i}}(D)(x) &= \bigvee_{i=1}^{l} \underline{Apr}_{d_{B_i}}(D_i)(x) \\ &\leq \bigvee_{i=1}^{l} \underline{Apr}_{d_{B_j}}(D_i)(x) \\ &= Pos_{d_{B_j}}(D)(x) \end{aligned}$$

(3.16f) For every $D_M = \{D_i \mid i \in M\} \subseteq D_N = \{D_i \mid i \in N\} \subseteq U/D$ and $x \in U$,

$$\begin{aligned} Pos_{d_B}(D_M)(x) &= \bigvee_{i=1}^{m} \underline{Apr}_{d_B}(D_i)(x) \\ &\leq \bigvee_{i=1}^{n} \underline{Apr}_{d_B}(D_i)(x) \\ &= Pos_{d_B}(D_N)(x) \end{aligned}$$

□

The theoretical framework of MFPR serves as a practical tool in image processing. During the image enhancement phase, MFPR is employed to identify critical regions in images that are essential for decision-making, referred to as target regions. Furthermore, the integration of sliding windows and PCNN algorithms facilitates the optimization of image feature quality, thereby improving classification accuracy. The following sections will provide a detailed discussion of the implementation steps for these techniques.

4. Image processing based on the MFPR algorithm

This section outlines the process of implementing the MFPR algorithm to optimize image feature quality, focusing on critical steps such as image segmentation, evaluation, and the generation of the optimal feature set.

4.1. Image segmentation and evaluation

This study uses a sliding window block algorithm for image partitioning to analyze the local information of the image. For an image of size (x, y), a rectangular window block of (l, w) is defined. The window block slides from left to right and from top to bottom with a specified step size λ, extracting image information [45]. The window block size and step size must be appropriately selected: excessively large blocks may obscure target features, while overly small blocks might capture insufficient features, hindering effective analysis. If λ is too large, the overlap between window blocks will decrease or disappear, affecting the relationship between the segmented blocks. In contrast, if λ is too small, the

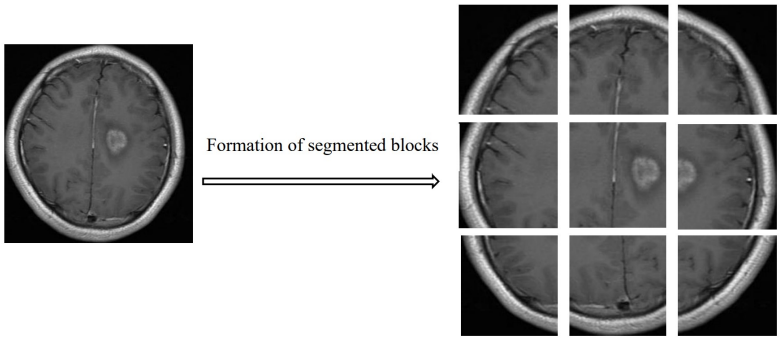

Figure 4. Sliding window block traversal for image segmentation.

traversal of the entire image will take a long time [33]. Given the varying resolutions of the images in the data set used in this experiment, fixed proportional relationships are applied to determine the dimensions of the sliding window blocks and step sizes. As shown in Figure 4, setting the sliding window to $\left(\frac{2x}{5}, \frac{2y}{5}\right)$ and setting the step size to $\left(\frac{x-l}{2}, \frac{y-w}{2}\right)$, traversing the entire image yields nine segmented blocks.

Subsequently, the GLCM is computed for each segmented block. When the gray-scale level of an image is too high, the resulting GLCM becomes excessively large, increasing computational complexity. Moreover, some gray-scale levels may occur infrequently or not at all, resulting in a sparse GLCM that can lead to inaccurate texture feature extraction. Therefore, before generating the GLCM, it is necessary to appropriately reduce the number of gray-scale levels in the original image. In this study, the gray-scale levels are reduced to 32 to balance computational efficiency and feature accuracy [2].

For a GLCM with dimensions $N_g \times N_g$, the sums of all elements in row i and column j of $G(i,j)$ are denoted respectively as:

$$p_x(i) = \sum_{j=0}^{N_g-1} p(i,j); \tag{4.1a}$$

$$p_y(j) = \sum_{i=0}^{N_g-1} p(i,j), \tag{4.1b}$$

where $p(i,j)$ is the normalized GLCM. Let $\mu_x, \mu_y, \sigma_x, \sigma_y$ be the means and standard deviations of $p_x(i)$ and $p_y(j)$ respectively. The extracted texture features are defined as follows [55]:

- Correlation (Cor) reflects the linear relationship between gray-levels in an image, with higher values indicating stronger linear correlations and lower values indicating weaker correlations.

$$Cor = \frac{\sum_{i=0}^{N_g-1}\sum_{j=0}^{N_g-1}(i\cdot j)\cdot p(i,j) - \mu_x \cdot \mu_y}{\sigma_x \cdot \sigma_y}. \tag{4.2}$$

- Contrast (Con) measures the degree of local variation within an image and reflects the differences between gray-scale levels, indicating the clarity and depth of texture.

$$Con = \sum_{i=0}^{N_g-1}\sum_{j=0}^{N_g-1}(i-j)^2 \cdot p(i,j). \tag{4.3}$$

- Entropy (Ent) measures the randomness in the information content of an image, reflecting the complexity of its gray-scale distribution. A higher entropy value

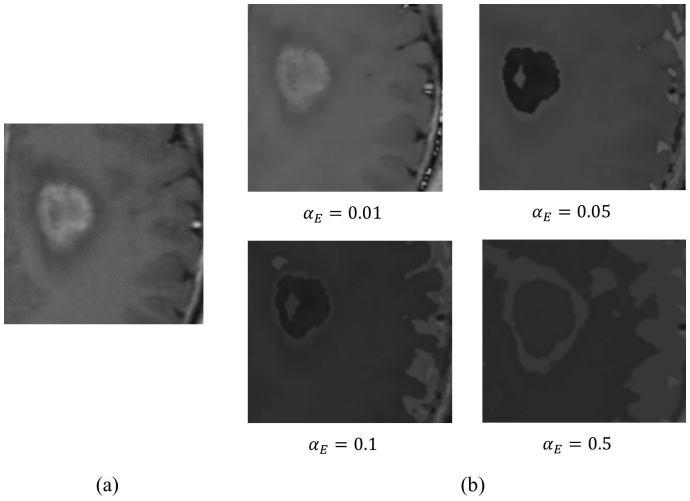

Figure 5. The enhancement effects correspond to different values of α_E.
(a) is the original image. (b) shows the images when α_E is 0.01, 0.05, 0.1, or 0.5.

indicates more complex image textures.

$$Ent = -\sum_{i=0}^{N_g-1}\sum_{j=0}^{N_g-1} p(i,j)\cdot\log(p(i,j)). \tag{4.4}$$

- Angular second moment (ASM) is a metric used to assess the uniformity of an image's gray-level distribution and the texture's coarseness or fineness, providing insight into irregular or complex texture patterns.

$$ASM = \sum_{i=0}^{N_g-1}\sum_{j=0}^{N_g-1} p(i,j)^2. \tag{4.5}$$

- Inverse difference moment (IDM) reflects the clarity and regularity of an image's texture. A higher value indicates greater texture clarity and stronger regularity.

$$IDM = \sum_{i=0}^{N_g-1}\sum_{j=0}^{N_g-1} \frac{1}{1+(i-j)^2}p(i,j). \tag{4.6}$$

In this study, a pixel distance of $d = 1$ is used to generate the GLCM at four orientations: 0 ř, 45 ř, 90 ř and 135 ř. Each GLCM extracts five texture features, resulting in a total of 20 features per image. Based on these features, the segmented block with the highest fuzzy positive region value is selected for subsequent enhancement using PCNN.

4.2. Generation of optimal feature set

From (2.5) and (2.6), it is observed that the time decay constant α_E directly influences the decay rate of the threshold voltage E_{ij} and the effectiveness of image enhancement. An appropriate value of α_E is crucial; too high values hinder noise removal, while too low values impair image details and edge enhancement. Figure 5 displays the results of the varying image enhancement with α_E values of 0.01, 0.05, 0.1 and 0.5, where Figure 5(a) is a segmented block of Figure 4. It is evident from the results that excessively low α_E values result in subtle image enhancements, while overly high values lead to distortion. Therefore, selecting an optimal α_E is critical to achieving high-quality enhancement outcomes.

To achieve optimal enhancement effects, a multi-round enhancement strategy is employed. The number of enhancement rounds for each MRI in the brain tumor dataset depends on the distinct values α_E. For example, increasing α_E from 0.01 to 0.5 in 0.01

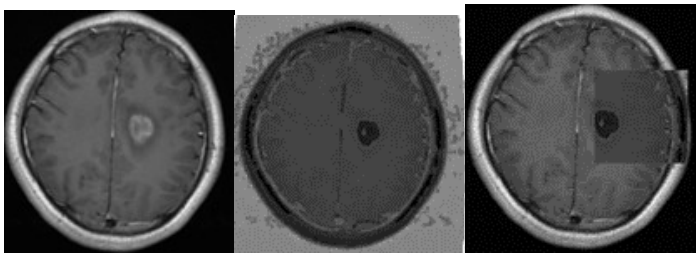

Figure 6. Display of glioma MRI under different image processing conditions. (a) Original image. (b) Global enhancement image. (c) Local enhancement image.

steps results in 50 iterations per MRI, producing a set of enhanced block candidates. As shown in Figure 6(c), blocks of the candidate set are progressively integrated into the original image to create locally enhanced images. The gray-level features of these images are extracted using GLCM, and the locally enhanced image with the highest fuzzy positive region value is selected as the optimal enhancement. Ultimately, the optimal feature set consists of the best-enhanced features from each image. Figure 6(b) shows the corresponding globally enhanced image. Compared to (b), (c) selectively enhances target areas, reducing noise interference and improving texture and contrast in key regions. When calculating the fuzzy positive region for a single locally enhanced image, the remaining images in the data set remain unchanged. The specific implementation process is outlined in Algorithm 1.

5. Experimental analysis

This experiment uses a dataset obtained from the open dataset "Brain Tumor Classification (MRI)" available on the Kaggle platform [6], which predominantly comprises three types of brain tumors:

- Gliomas [23], primarily originating from glial cells in the brain or spinal cord, represent one of the most common types of primary brain tumors. They typically present with irregular borders and shapes in MRI, with locations that vary significantly.
- Meningiomas [47], typically originating from the membranes surrounding the brain or spinal cord, can compress adjacent brain tissue and nerves, leading to various neurological symptoms. They usually appear as round or oval shapes in MRI, with relatively distinct boundaries.
- Pituitary tumors [7], which originate in the pituitary gland, typically cause enlargement of the pituitary region. Their MRI characteristics vary depending on their size, type, and hormone secretion status.

To ensure generalizability of the experimental results, 12 classification models were selected and grouped into six categories based on their underlying classification principles:

- Tree-based classifiers: Gradient Boosting (GB), Decision Tree (DT), CatBoost, ExtraTrees (ET), XGBoost, and LightGBM.
- Distance-based classifier: K-Nearest Neighbors (KNN).
- Kernel technique for non-linear data: Support Vector Classifier (SVC).
- Probabilistic classification: Gaussian Naive Bayes (GNB).
- Linear Classifiers: Logistic Regression (LR).
- Performance enhancement through the model ensemble: AdaBoost, Bootstrap Aggregating (BA).

Algorithm 1 Optimizing Image Features by MFPR

Require: Images: Image dataset
num: Total number of iterations for time decay constant α_E transformation
Ensure: A_{best}: Optimal feature set
Perform denoising preprocessing on Images;
$A_0 \leftarrow$ Extract feature set using GLCM from all original Images;
Initialize: $v = 0$, $n = |\text{Images}|$, $i = 1$;
Local Enhancement:
while $i \leq$ num **do**
  for $j = 1$ to n **do**
    Segment the j-th image into m blocks using sliding window block algorithm;
    for $l = 1$ to m **do**
      $a_{jl} \leftarrow$ Extract features from the l-th block of j-th image using GLCM;
      $A_{jl} \leftarrow$ Update features of j-th image in A_0 to a_{jl};
      $p_{jl} \leftarrow$ Calculate MFPR value of A_{jl};
      if $p_{jl} > v$ **then**
        $v \leftarrow p_{jl}$;
        $l_b \leftarrow l$;
      end if
    end for
    Enhance l_b-th block of j-th image using PCNN;
    Embed enhanced block into j-th image to form locally enhanced image;
  end for
  $A_i \leftarrow$ Extract features from all locally enhanced images using GLCM;
  $i \leftarrow i + 1$;
end while
Feature Fusion:
while $j \leq n$ **do**
  for $i = 1$ to num **do**
    $a_{ij} \leftarrow$ Features of j-th image in A_i;
    $A_{ij} \leftarrow$ Update features of j-th image in A_0 to a_{ij};
    $p_{ij} \leftarrow$ Calculate MFPR value of A_{ij};
    if $p_{ij} > v$ **then**
      $v \leftarrow p_{ij}$;
      $i_b \leftarrow i$;
    end if
  end for
  $j \leftarrow j + 1$;
  Set features of j-th image in A_{best} to $a_{i_b j}$;
end while

Different classifiers may exhibit substantial performance differences in the same dataset. By comparing multiple classifiers, the data can be analyzed comprehensively from various perspectives, thereby validating the generalizability of the algorithms. In this experiment, 100 images were randomly selected from each of the three categories of brain tumors, totaling 300 images. During the pre-processing stage, all images underwent denoising and normalization, followed by processing using the Original, GE, SFPR, and MFPR algorithms, respectively. To evaluate the generalization capability, the classification performance of 12 models was tested under these four processing methods. To ensure a fair comparison among the algorithms, both data partitioning and model configurations were standardized. Specifically, stratified random sampling with a fixed seed (`random_state=3220819`) was

Table 2. Experimental parameters configuration table

Method	**Parameters**
Sliding window blocks	1. Size: $\frac{2\cdot x}{5} \times \frac{2\cdot y}{5}$ 2. Step length λ: $\frac{x-l}{3} \times \frac{y-w}{3}$
GLCM	1. Gray-level: 32 levels 2. Distance $d = 1$ 3. Angles θ: 0°, 45°, 90°, 135°
PCNN	1. Potential $V_L = 1.00$ 2. Decay $\alpha_L = 0.06931$ 3. Strength $\beta = 0.2$ 4. Amplitude $V_E = 200$ 5. Decay $\alpha_E = 0.01$ 6. Updates for α_E: $m = 50$ 7. Pulse ignitions $n = 1000$
Metric function	$d_b(x, y) = \lvert b(x) - b(y)\rvert$

employed to split the dataset into training (70%) and testing (30%) subsets. Moreover, all classification models were executed with their default hyperparameter settings throughout the experiments, thereby minimizing potential performance biases arising from variations in parameter optimization. All experimental results documented in Tables 35 strictly adhere to this protocol. The classification results were evaluated using three metrics: confusion matrix, classification accuracy, and kappa coefficient. Furthermore, the effect of different segmentation block sizes on the performance of the proposed algorithm was investigated. All algorithms were implemented in Python 3.11.5 and executed on a hardware platform equipped with a 12th Gen Intelő Core i9-12900H @ 2.50GHz processor and 32GB of RAM. Comprehensive parameter specifications are provided in Table 2.

5.1. Evaluation of classification performance

This section primarily evaluates the experimental results from three aspects: confusion matrix, classification accuracy and kappa coefficient.

5.1.1. Confusion matrix. The confusion matrix is a commonly used tool for evaluating classification performance. Visualizes the distribution of data within true classes during prediction in tabular form. In a confusion matrix, the columns represent the actual classes and the rows represent the predicted classes. False negatives and false positives are key metrics in the confusion matrix to evaluate model performance. False negatives refer to target-class images that are misclassified into other classes, while false positives refer to images from other classes that are misclassified as the target class. From the confusion matrix, several performance metrics can be calculated, such as classification accuracy, precision, recall, and F1 score, providing a comprehensive assessment of feature extraction performance under different algorithms. ,

In this section, the CatBoost classification model is used to obtain the confusion matrices for the features extracted based on the original algorithms, GE, MFPR, and SFPR. The size of the sliding window is set to $(\frac{2x}{5}, \frac{2y}{5})$ with a step size λ of $(\frac{x-l}{3}, \frac{y-w}{3})$. As shown in Table 3, the MFPR algorithm demonstrated a classification accuracy of 90.00%, showing a significant advantage over other comparative algorithms. Furthermore, compared to the original, GE and SFPR algorithms, the MFPR algorithm exhibited poor misclassification rates in both glioma and meningioma, with only 1 false negative and 0 false positives in glioma. Although the number of false negatives increased for the pituitary tumor, the MFPR algorithm significantly reduced the number of false positives. In summary, the

Table 3. Confusion matrix and classification accuracy under four algorithms using the CatBoost classifier

Original (Accuracy = 82.22%)				**GE (Accuracy = 85.56%)**			
	glioma	meningioma	pituitary		glioma	meningioma	pituitary
glioma	20	5	7	glioma	27	3	2
meningioma	1	28	2	meningioma	3	26	2
pituitary	1	0	26	pituitary	3	0	24
SFPR (Accuracy = 87.78%)				**MFPR (Accuracy = 90.00%)**			
	glioma	meningioma	pituitary		glioma	meningioma	pituitary
glioma	29	1	2	glioma	31	0	1
meningioma	0	27	4	meningioma	0	28	3
pituitary	0	4	23	pituitary	0	5	22

MFPR algorithm not only improves overall classification accuracy but also reduces the risk of misdiagnosis in brain tumors, providing more stable and reliable performance when handling complex and variable data sets. Table 4 and Table 5 use the same parameter configurations.

5.1.2. Classification accuracy. To more reliably evaluate the impact of different algorithms on classification performance, we calculated the classification accuracy of 12 classifiers on datasets processed by the original, GE, MFPR and SFPR algorithms. The proposed MFPR algorithm was compared with the other three algorithms using three symbols: higher (v), equal (*), or lower (), as shown in Table 4. The symbol "higher (v)" indicates that within the same classifier, the features extracted using the MFPR algorithm exhibit superior performance compared to those extracted by the other algorithms. For example, in the DT classifier, the features extracted using the MFPR algorithm demonstrated superior performance compared to those derived from the SFPR algorithm and the original data, while performing comparably to the GE algorithm. The final row of the table summarizes the counts of these comparison outcomes. For example, the value "(10/2/0)" in the last row for GE means that the MFPR algorithm outperformed GE in 10 classifiers, performed equally to GE in 2 classifiers and performed worse in 0 classifiers. The results consistently demonstrate that the MFPR algorithm outperforms the three comparative algorithms in terms of classification accuracy. Moreover, the MFPR algorithm achieved classification accuracies that exceeded 85% between classifiers such as KNN, LightGBM, BA, GB, XGBoost, ET and CatBoost. Comprehensive comparative analyzes further demonstrate that the MFPR algorithm significantly enhances image feature quality, thereby improving classification accuracy.

5.1.3. Kappa coefficient. The kappa coefficient is another crucial metric for evaluating classification performance [32]. Unlike accuracy, which directly evaluates performance, the kappa coefficient measures the agreement between model predictions and actual results, providing a more precise evaluation, especially in cases of class imbalance. A higher kappa coefficient indicates better classification consistency and less randomness. Using both accuracy and the kappa coefficient, a more comprehensive assessment of algorithm performance is provided. Table 5 presents the kappa coefficients of the 12 classification models on the data processed by the four algorithms. The MFPR algorithm significantly outperforms the other three algorithms in both consistency and predictive accuracy. Moreover, the kappa coefficients for the MFPR algorithm in various classification models consistently exceed 60%.

Table 4. Classification accuracy across 12 different models

Model	MFPR	SFPR	GE	Original
KNN	90.00%	83.33%v	86.67%v	76.67%v
DT	82.22%	73.33%v	82.22%*	78.89%v
LR	73.33%	68.89%v	48.89%v	71.11%v
GNB	75.56%	66.67%v	61.11%v	67.78%v
LightGBM	88.89%	81.11%v	85.56%v	84.44%v
AdaBoost	83.33%	72.22%v	81.11%v	77.78%v
BA	86.67%	81.11%v	83.33%v	78.89%v
GB	87.78%	80.00%v	84.44%v	81.11%v
SVC	76.67%	71.11%v	46.67%v	70.00%v
XGBoost	85.56%	78.89%v	85.56%*	83.33%v
ET	90.00%	83.33%v	83.33%v	77.78%v
CatBoost	90.00%	87.78%v	85.56%v	82.22%v
summary	(v/*/^)	(12/0/0)	(10/2/0)	(12/0/0)

Table 5. Kappa coefficients across 12 different models

Model	MFPR	SFPR	GE	Original
KNN	85.00%	74.90% v	80.00% v	65.10% v
DT	73.30%	60.10% v	73.20% v	68.40% v
LR	59.90%	53.00% v	24.50% v	57.10% v
GNB	62.80%	49.20% v	41.60% v	52.50% v
LightGBM	83.30%	71.60% v	78.20% v	76.70% v
AdaBoost	74.90%	58.50% v	71.60% v	66.80% v
BA	79.90%	71.50% v	74.90% v	68.40% v
GB	81.70%	70.00% v	76.60% v	71.70% v
SVC	64.60%	56.10% v	22.90% v	55.60% v
XGBoost	78.30%	68.30% v	78.20% v	75.10% v
ET	84.90%	74.90% v	75.00% v	66.90% v
CatBoost	85.00%	81.70% v	78.30% v	73.50% v
summary	(v/*/^)	(12/0/0)	(12/0/0)	(12/0/0)

5.2. Analysis of results under different sizes of sliding window blocks

To rigorously evaluate the performance of the proposed algorithm, sliding window blocks with five distinct dimensions $(\frac{2x}{5}, \frac{2y}{5})$, $(\frac{3x}{8}, \frac{3y}{8})$, $(\frac{4x}{8}, \frac{4y}{8})$, $(\frac{5x}{8}, \frac{5y}{8})$, and $(\frac{6x}{8}, \frac{6y}{8})$ were applied, with the stride parameter λ uniformly configured as $(\frac{x-l}{3}, \frac{y-w}{3})$ during sliding window operations. To eliminate interference from classifier performance variations, the classification accuracy of all algorithms was computed using the ET classifier. This classifier demonstrated superior stability in preliminary experiments (see Table 4), thus ensuring that the experimental results (see Figure 7) directly reflect the robustness of the MFPR algorithm under varying window sizes. As shown in Figure 7, the MFPR algorithm consistently outperforms the others in all sliding window sizes, demonstrating superior robustness and performance. Moreover, the choice of window size significantly impacts the quality of the extracted feature sets.

In general, the experimental analysis in Section 5 demonstrates that the MFPR algorithm exhibits significant advantages over the original, GE, and SFPR algorithms in all

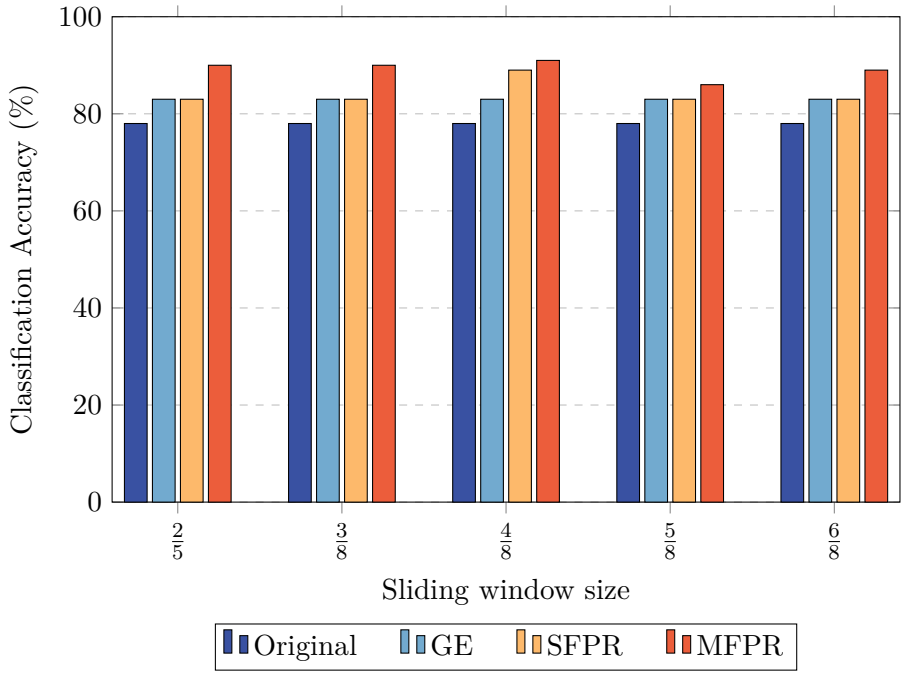

Figure 7. Classification accuracy of four algorithms with various window sizes using the ET classifier.

evaluation metrics. The MFPR algorithm outperforms superior performance based on metric-based fuzzy positive regions compared to similarity-based fuzzy positive regions, enabling a more accurate selection of segmentation blocks with greater decision relevance. Furthermore, the classification results for the varying sizes of the sliding windows reveal that the feature data sets extracted using the MFPR algorithm consistently achieve higher classification accuracy. These results also indicate that locally enhancing segmentation blocks with high decision relevance effectively improves the feature quality of the data set.

6. Conclusion

Enhancing the accuracy of the brain tumor MRI classification is crucial to improving patient survival rates. Early and precise diagnosis and classification allow physicians to develop more effective treatment plans and reduce the risk of recurrence. Therefore, the development of efficient image feature optimization algorithms is essential for the early diagnosis of brain tumors.

This paper presents an MFPR-based optimization algorithm for MRI feature extraction from brain tumors. The algorithm addresses the limitations of traditional methods in both feature extraction and image enhancement while simultaneously increasing classification performance. By evaluating the significance of each window block through the MFPR metric, it accurately identifies the optimal regions for enhancement. Regions with higher fuzzy positive region values typically contain more decision-critical details; enhancing these areas significantly improves image contrast and detail representation. The experimental results confirm that the proposed algorithm not only enhances the quality of the features but also outperforms the original, GE, and SFPR algorithms in terms of classification accuracy and stability. Consequently, this algorithm offers valuable insights for clinicians and serves as a reliable decision-support tool for early brain tumor diagnosis. Furthermore, its capability to enhance decision-critical regions while maintaining computational efficiency makes it particularly advantageous in scenarios with limited training data, a

common challenge in medical imaging. However, further refinement and expansion of the algorithm remain promising directions for future research.

Firstly, since the performance of this algorithm is highly dependent on the configuration of the sliding window size and step length, different tumor types may require specific sliding window parameters to ensure optimal feature extraction and enhancement. Therefore, future research could focus on developing more refined methods for tuning the sliding window parameters, tailored to different types of tumors. For instance, exploring adaptive window adjustment techniques or dynamic parameter optimization strategies based on image content could enhance the algorithm's adaptability and robustness across diverse applications.

Secondly, while this study has focused on the optimization of features for brain tumor MRI images, the potential clinical applications of the proposed approach are not limited to MRI. Future research could explore its application in other medical imaging modalities, such as CT scans, X-ray images, and histopathology images. Adapting the algorithm to these modalities could address the unique challenges posed by different imaging techniques and further enhance diagnostic accuracy in a broader range of clinical settings. This extension would not only provide a more comprehensive evaluation of the versatility of the algorithm but would also contribute to the integration of multimodal imaging data in clinical decision making.

Finally, machine learning is inherently limited in handling complex high-dimensional data, so the proposed algorithm is generally not superior to deep learning-based brain tumor classification algorithms in terms of time efficiency and classification accuracy. However, deep learning algorithms rely on large amounts of input data, which is a limiting factor when sample data is scarce. In contrast, the MFPR algorithm excels at analyzing differences between elements in images with ambiguous and incomplete information, which is a key advantage. Future research could integrate the strengths of the MFPR algorithm with the highly efficient automated processing capabilities of deep learning. This approach has the potential to reduce the reliance of deep learning on extensive labeled data sets and facilitate the development of more advanced brain tumor classification or segmentation algorithms.

Author contributions. All the co-authors have contributed equally in all aspects of the preparation of this submission.

Conflict of interest statement. The authors declare that they have no known competing financial interests or personal relationships that could have appeared to influence the work reported in this paper.

Funding. This research was funded by the National Natural Science Foundation of China (Nos.12371462) and the Fundamental Research Funds for the Central Universities (No. 2019zy20).

Data availability. The data used in this study are publicly available in the "Brain Tumor Classification (MRI)" open dataset on the Kaggle platform, accessible at [DOI: 10.34740/KAGGLE/DSV/1183165].

References

[1] A.I. Awad, *Machine learning techniques for fingerprint identification: A short review*, Lect. Notes Comput. Sci. **322**, 524–531, 2012.

[2] A. Alsalihi, H.K. Aljobouri and E.A.K. Altameemi, *GLCM and CNN deep learning model for improved MRI breast tumors detection*, Int. J. Online Biomed. Eng. **18**, 123–137, 2022.

[3] S. Banach, *Théorie des opérations linéaires*, Warsaw 1932.

[4] Z. Bonikowski, E. Bryniarski and U. Wybraniec-Skardowska, *Extensions and intentions in the rough set theory*, Inf. Sci. **107** (1-4), 149–167, 1998.
[5] S. Basak, R. Jia and C. Lei, *Face recognition using fuzzy logic*, Proc. IEEE Int. Conf. Inf. Autom. 1317–1322, 2018.
[6] S. Bhuvaji, A. Kadam, P. Bhumkar, S. Dedge and S. Kanchan, *Brain tumor classification (MRI)*, Kaggle 2020.
[7] B. Bahuleyan, L. Raghuram, V. Rajshekhar and A.G. Chacko, *To assess the ability of MRI to predict consistency of pituitary macroadenomas*, Br. J. Neurosurg. **20** (5), 324–326, 2006.
[8] L. Chen and Q. Chen, *A novel classification algorithm based on kernelized fuzzy rough sets*, Int. J. Mach. Learn. Cybern. **11** (12), 2565–2572, 2020.
[9] G. Chen and Z.S. Chen, *Regional classification of urban land use based on fuzzy rough set in remote sensing images*, J. Intell. Fuzzy Syst. **38** (3), 3803–3812, 2020.
[10] V. Chirchi, E. Chirchi and K.E. Chirchi, *Pattern matching for the iris biometric recognition system uses KNN and fuzzy logic classifier techniques*, Int. J. Inf. Technol. **16** (4), 2937–2944, 2024.
[11] X.F. Cheng, X.J. Li and X.D. Ma, *A method for battery fault diagnosis and early warning combining isolated forest algorithm and sliding window*, Energy Sci. Eng. **11** (12), 4493–4504, 2023.
[12] Y. Chen, S.K. Park, Y. Ma and R.K. Ala, *A new automatic parameter setting method of a simplified PCNN for image segmentation*, IEEE Trans. Neural Netw. **22** (6), 880–892, 2011.
[13] J. Cheng, W. Yang, M. Huang, W. Huang, J. Jiang, Y. Zhou, R. Yang, J. Zhao, Y. Feng, Q. Feng and W. Chen, *Retrieval of brain tumors by adaptive spatial pooling and fisher vector representation*, PLoS ONE **11** (6), e0157112, 2016.
[14] Y. Du, Q. Hu, D.G. Chen and P. Ma, *Kernelized fuzzy rough sets based yawn detection for driver fatigue monitoring*, Fundam. Inform. **111** (1), 65–79, 2011.
[15] A. Eleyan and H. Demirel, *Co-occurrence matrix and its statistical features as a new approach for face recognition*, Turk. J. Electr. Eng. Comput. Sci. **19** (2), 285–295, 2011.
[16] E.A. El-Dahshan, H.M. Mohsen, K. Revett and A.M. Salem, *Computer-aided diagnosis of human brain tumor through MRI: A survey and a new algorithm*, Expert Syst. Appl. **41** (11), 5526–5545, 2014.
[17] S.F. Farahbakhshian and M.T. Ahvanooey, *A new gene selection algorithm using fuzzy-rough set theory for tumor classification*, Control Eng. Appl. Inform. **22** (1), 14–23, 2020.
[18] M. Fatima and M. Pasha, *Survey of machine learning algorithms for disease diagnostic*, J. Intell. Learn. Syst. Appl. **9** (1), 1–16, 2017.
[19] T. Feng, S. Zhang and J. Mi, *The reduction and fusion of fuzzy covering systems based on the evidence theory*, Int. J. Approx. Reason. **53** (1), 87–103, 2012.
[20] J. Goubault-Larrecq, *Non-Hausdorff topology and domain theory*, Cambridge University Press 2013.
[21] X. Gu, *Research on pulse coupled neural networks and their applications*, Science Press, Beijing, 2003.
[22] H.W. Goo and Y.S. Ra, *Advanced MRI for pediatric brain tumors with emphasis on clinical benefits*, Korean J. Radiol. **18** (1), 194–207, 2017.
[23] N. Haydar, K. Alyousef, U. Alanan, R. Issa, F. Baddour, Z. Al-shehabi and M.H. Al-janabi, *Role of magnetic resonance imaging (MRI) in grading gliomas comparable with pathology: A cross-sectional study from Syria*, Ann. Med. Surg. **82**, 104679, 2022.
[24] R.M. Haralick, K. Shanmugam and I. Dinstein, *Textural features for image classification*, IEEE Trans. Syst. Man Cybern. **SMC-3** (6), 610–621, 1973.
[25] G. Kuntimad and H.S. Ranganath, *Perfect image segmentation using pulse coupled neural networks*, IEEE Trans. Neural Netw. **10** (3), 591–598, 1999.

[26] L. Kong, J. Zhang, Y. Wang, C. Zhang and Q. Hu, *Distributed feature selection for big data using fuzzy rough sets*, IEEE Trans. Fuzzy Syst. **28** (5), 846–857, 2020.
[27] S. Liu, *Study on medical image enhancement based on wavelet transform fusion algorithm*, J. Med. Imaging Health Inform. **7** (2), 388–392, 2017.
[28] L.Y. Liu and X.J. Fan, *The design of system to texture feature analysis based on gray level co-occurrence matrix*, Appl. Mech. Mater. **727-728**, 904–907, 2015.
[29] T. Lindblad and J.M. Kinser, *Image processing using pulse-coupled neural networks*, Springer, London, 1998.
[30] J. Lee, S.R. Pant and H. Lee, *An adaptive histogram equalization based local technique for contrast preserving image enhancement*, Int. J. Fuzzy Log. Intell. Syst. **15** (1), 35–44, 2015.
[31] L. Lei, F. Xi and S. Chen, *Finger-vein image enhancement based on pulse coupled neural network*, IEEE Access **7**, 57226–57237, 2019.
[32] M.L. McHugh, *Interrater reliability: The kappa statistic*, Biochem. Med. **22** (3), 276–282, 2012.
[33] R. Membarth, O. Reiche, F. Hannig, J. Teich, M. Körner and W. Eckert, *HIPAcc: A domain-specific language and compiler for image processing*, IEEE Trans. Parallel Distrib. Syst. **27** (1), 210–224, 2016.
[34] R. Nie, M. He, J. Cao, D. Zhou and Z. Liang, *Pulse coupled neural network based MRI image enhancement using classical visual receptive field for smarter mobile healthcare*, J. Ambient Intell. Humaniz. Comput. **10** (8), 3345–3357, 2019.
[35] F.J. Provost, *On applied research in machine learning*, Proc. Conf. Appl. Res. Mach. Learn. 1–8, 1998.
[36] Y. Qu, Q. Fu, C. Shang, A. Deng, R. Zwiggelaar, M. George and Q. Shen, *Fuzzy-rough assisted refinement of image processing procedure for mammographic risk assessment*, Appl. Soft Comput. **91**, 106230, 2020.
[37] Y. Qu, C. Shang, Q. Shen, N. MacParthaláin and W. Wu, *Kernel-based fuzzy-rough nearest-neighbour classification for mammographic risk analysis*, Int. J. Fuzzy Syst. **17** (3), 471–483, 2015.
[38] Y. Qu, G. Yue, C. Shang, L. Yang, R. Zwiggelaar and Q. Shen, *Multi-criterion mammographic risk analysis supported with multi-label fuzzy-rough feature selection*, Artif. Intell. Med. **100**, 101722, 2019.
[39] U. Raghavendra, A. Gudigar, A. Paul, T.S. Goutham, M.A. Inamdar, A. Hegde, A. Devi, C.P. Ooi, R.C. Deo, P.D. Barua, F. Molinari, E.J. Ciaccio and U.R. Acharya, *Brain tumor detection and screening using artificial intelligence techniques: Current trends and future perspectives*, Comput. Biol. Med. **163**, 107063, 2023.
[40] U. Reddy, B.V.R. Reddy and B.E. Reddy, *Categorization & recognition of lung tumor using machine learning representations*, Curr. Med. Imaging Rev. **15** (4), 405–413, 2019.
[41] C.K. Sirajuddeen, S. Kansal and R.K. Tripathi, *Adaptive histogram equalization based on modified probability density function and expected value of image intensity*, Signal Image Video Process. **14** (1), 9–17, 2020.
[42] J. Shi, Y. Lei, J. Wu and G. Jeon, *Uncertain active contour model based on rough and fuzzy sets for auroral oval segmentation*, Inf. Sci. **492**, 72–103, 2019.
[43] M.M. Subashini and S.K. Sahoo, *Pulse coupled neural networks and its applications*, Expert Syst. Appl. **41** (8), 3965–3974, 2014.
[44] R. Sowiski and D. Vanderpooten, *A generalized definition of rough approximations based on similarity*, IEEE Trans. Knowl. Data Eng. **12** (3), 331–336, 2000.
[45] R.B. Vallabhaneni and V. Rajesh, *Brain tumour detection using mean shift clustering and GLCM features with edge adaptive total variation denoising technique*, Alex. Eng. J. **57** (4), 2387–2392, 2018.

[46] M.J. Warrens, *Weighted kappa is higher than Cohen's kappa for tridiagonal agreement tables*, Stat. Methodol. **8** (2), 268–272, 2011.

[47] J. Watts, G.A. Box, A. Galvin, P.R. Brotchie, N.M. Trost and T.R. Sutherland, *Magnetic resonance imaging of meningiomas: A pictorial review*, Insights Imaging **5** (1), 113–122, 2014.

[48] Q. Wang and R.K. Ward, *Fast image/video contrast enhancement based on weighted thresholded histogram equalization*, IEEE Trans. Consum. Electron. **53** (2), 757–764, 2007.

[49] F.X. Wu and X.B. Zhang, *An enhanced method of color image combined PCNN based on NSCT*, J. Ambient Intell. Humaniz. Comput. **7** (6), 1597–1608, 2016.

[50] X. Xu, G. Wang, S. Ding, Y. Cheng and X. Wang, *Pulse-coupled neural networks and parameter optimization methods*, Neural Comput. Appl. **28** (1), 671–681, 2017.

[51] W. Yao, Y. She and L.X. Lu, *Metric-based L-fuzzy rough sets: Approximation operators and definable sets*, Knowl.-Based Syst. **163**, 91–102, 2019.

[52] W. Yao, G.X. Zhang and C.J. Zhou, *Real-valued hemimetric-based fuzzy rough sets and an application to contour extraction of digital surfaces*, Fuzzy Sets Syst. **459**, 201–219, 2022.

[53] W. Zhu, H. Jiang, E. Wang, Y. Hou, L. Xian and J. Debnath, *X-ray image global enhancement algorithm in medical image classification*, Discrete Contin. Dyn. Syst. Ser. S **12** (4-5), 1297–1309, 2019.

[54] X. Zhang, C. Mei, J. Li, Y. Yang and T. Qian, *Instance and feature selection using fuzzy rough sets: A bi-selection approach for data reduction*, IEEE Trans. Fuzzy Syst. **31** (6), 1981–1994, 2023.

[55] N. Zulpe and V.P. Pawar, *GLCM textural features for brain tumor classification*, Int. J. Comput. Sci. Inf. Technol. **3** (3), 4138–4141, 2012.

[56] D. Zhou, H. Zhou, C. Gao and Y. Guo, *Simplified parameters model of PCNN and its application to image segmentation*, Pattern Anal. Appl. **19** (4), 939–951, 2016.